Deposition of Highly Porous Nanocrystalline Platinum on Functionalized Substrates Through Fluorine-Induced Decomposition of Pt(PF$_3$)$_4$ Adsorbates

Steven J. Randolph,*,[†] Aurelien Botman,[†] and Milos Toth[‡]

FEI Company, 5350 NE Dawson Creek Drive, Hillsboro, OR 97214-5793 USA, and School of Physics and Advanced Materials, University of Technology, Sydney, P.O. Box 123, Broadway, New South Wales 2007, Australia

Received July 18, 2013; E-mail: steven.randolph@fei.com

Highly porous, nanostructured platinum[1–5] has numerous applications in fuel cell technology,[4,6,7] gas sensing,[8,9] heterogeneous catalysis[10,11] and neurostimulation.[12,13] Most favorable properties arise from a combination of high catalytic activity and large surface-to-volume ratio. Pt synthesis methods[1,2] include chemical reduction (e.g., electrochemical, photochemical, sonochemical and radiolytic), thermal decomposition, ligand displacement from organometallics, hydrothermal growth, the sol-gel process, gas-mediated electron,[14,15] ion[15] and laser[16] beam induced deposition, laser ablation, chemical vapor deposition, and thermal evaporation. Porous platinum may also be produced[1] using dealloying methods and by chemical plating[17] or physical vapor deposition[18] onto a pre-existing, high porosity framework. Fabrication of porous Pt electrodes in device structures often requires additional processing steps such as fixation, screen or inkjet printing, spraying or casting of Pt nanocrystallites.[1]

Here we demonstrate a fluorine mediated process for the decomposition of gaseous Pt(PF$_3$)$_4$ into porous platinum comprised of nanocrystallites with a diameter of ∼ 3 nm and the morphological structure[19–22] of Pt black and Pt sponge. Film growth is achieved by flowing Pt(PF$_3$)$_4$ and XeF$_2$ vapors over a solid substrate in vacuum. The Pt nucleation time scales with the coverage of fluorine supplied through dissociative chemisorption of XeF$_2$. Subsequent, rapid film growth is autocatalyzed by highly pure, growing Pt nanocrystallites. Fluorine coverage is controlled by pre-dosing the substrate with XeF$_2$ and by optional, concurrent irradiation using an electron beam or an ion beam. The beams can be used to limit Pt nucleation to regions that are functionalized through locally enhanced fluorination, and to direct write Pt pads onto complex substrates such as metal-oxide composites used in device structures.

Benefits of the fabrication technique described here stem from the fact that it is rapid, solvent-free, does not require heating, pressurization, sonication or electrical connections, and produces gas phase byproducts which desorb rapidly during growth. The beam directed localization process is analogous to electron beam induced deposition (EBID) and ion beam induced deposition (IBID) which entail decomposition of surface-adsorbed growth precursors such as Pt(PF$_3$)$_4$ directly by the beams rather than by fluorine. However, EBID and IBID are many orders of magnitude slower than the technique presented here, and typically yield highly impure deposits.[14,15,23–26]

Film growth was achieved by injecting Pt(PF$_3$)$_4$ and XeF$_2$ vapors simultaneously into a vacuum chamber equipped with a co-incident focused Ga ion beam and a scanning electron microscope (SEM). Figure 1A shows SEM images of gas injection capillaries used to mix the precursors near a Si substrate (with a native oxide), and the time evolution of a film growing on the surface. Growth proceeds from the region of high XeF$_2$ flux toward the Pt(PF$_3$)$_4$ capillary, indicating a fluorine-limited reaction rate (SEM was used

for imaging, but growth also occurs in the absence of electron irradiation). The deposited film extends over one millimeter in the plane of the support, and has a thickness of several microns in the high gas flux region and tens of nanometers at the deposit periphery. Visual inspection of the Pt films revealed a dull-grey to nearly black appearance. Atomic force microscopy (AFM) topographic maps (Figure 1B) show a high degree of surface roughness and porosity at both the nano and micro scales.

The composition of the Pt(PF$_3$)$_4$ + XeF$_2$ reaction product was compared to that of high purity reference Pt, and impure nanocrystalline Pt fabricated by EBID using Pt(PF$_3$)$_4$ as the precursor gas[27–31] (in the absence of XeF$_2$). EBID typically produces materials with a high concentration of impurities comprised of precursor ligand constituents, and residual molecules such as H$_2$O and O$_2$ present in the vacuum chamber.[14,15,23–26] This issue is evidenced by the energy dispersive x-ray spectroscopy (EDS) data shown in Figure 1B. The EBID-grown film contains P, F and O impurities.[32] In contrast, the spectrum from the film grown by mixing Pt(PF$_3$)$_4$ with XeF$_2$ is indistinguishable from that of the reference, high purity Pt sample.
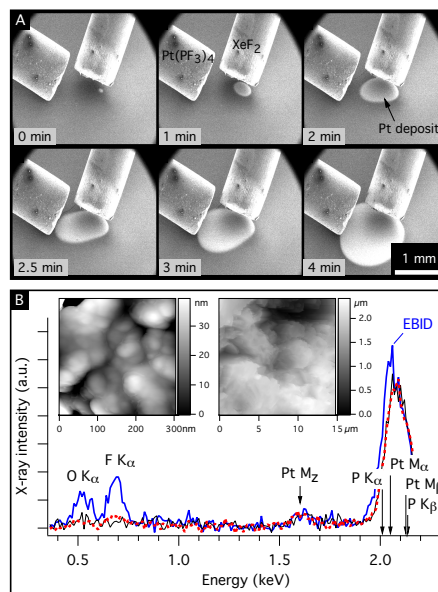

Figure 1. A) Time lapse sequence of SEM images showing gas delivery capillaries and Pt growth on a Si substrate. B) AFM topographic maps and an EDS spectrum of the Pt(PF$_3$)$_4$ + XeF$_2$ reaction product (······). The spectrum is compared to those of a reference, high purity Pt sample (———), and Pt deposited using EBID (———). The spectra are normalized to emphasize compositional differences between the three materials. Arrows show nominal x-ray line positions.

Critically, a conditioning period of at least 30 to 45 minutes of XeF$_2$ flow was needed at the start of each experimental session to achieve reproducible Pt nucleation behavior during simultaneous Pt(PF$_3$)$_4$ and XeF$_2$ flow.[33] This prerequisite is attributed to fluori-

[†]FEI

[‡]UTS

nation of the substrate through activated dissociative chemisorption of XeF_2, and the need for a fluorine-rich stoichiometry to achieve complete decomposition of $Pt(PF_3)_4$ adsorbates. It is well known[34–36] that XeF_2 dissociates on many surfaces, generating Xe (which desorbs rapidly) and chemisorbed fluorine, and that the fluorine concentration takes tens of minutes to saturate and reach one monolayer on SiO_2[37] at room temperature. It is also well established that electron exposure causes dissociation of XeF_2 adsorbates, and that the resulting fluorine can chemisorb to the substrate.[38] It is therefore reasonable to expect that electron beam pre-exposure of a substrate in an XeF_2 environment may increase the fluorine coverage and localize Pt film growth. To test this hypothesis, three 50 μm partially overlapping circles were patterned in parallel on the native oxide of a Si substrate with an electron beam. The electron fluence was maintained sufficiently low to prevent removal of the oxide by electron beam induced etching[38,39] and avoid rapid spontaneous[34,35] XeF_2 etching of the Si. Following pre-patterning, the beam was blanked, $Pt(PF_3)_4$ was injected into the chamber, and the precursors were flown simultaneously for $\sim$ 60 s. The substrate was imaged using secondary electrons and the Pt M_α and Si K_α x-ray lines (Figure 2A) immediately after cessation of precursor flow. Clearly, the Pt deposited only in regions that had been pre-patterned by the beam, and the quantity of Pt scales with pre-exposure electron fluence.

It is important to emphasize that the beam-induced-fluorination process reduces the Pt nucleation time, but the subsequent deposition rate is constant and independent of the electron fluence. The contrast in the Pt M_α map seen in Figure 2A is caused by corresponding variations in nucleation time and hence the net Pt growth time. Film localization was maintained by making the XeF_2 partial pressure sufficiently low to delay nucleation in regions that had not been pre-patterned beyond the total Pt deposition time. After nucleation, rapid, localized Pt growth was observed, indicative of an autocatalytic process mediated by high purity Pt. Conversely, all attempts at localization failed when $Pt(PF_3)_4$ and XeF_2 were flown over substrates that contained deposits which had been pre-grown by EBID. This is consistent with the EDS spectra in Figure 1B which show that the EBID-grown material contains impurities that likely inhibit Pt growth autocatalysis.

Localized deposition of the highly pure Pt films can also be achieved by scanning a substrate while $Pt(PF_3)_4$ and XeF_2 are delivered to the vacuum chamber. A Pt pad grown using this approach is shown in Figure 2B where the substrate is a metal-oxide composite comprised of thermal SiO_2 and Cr electrodes. The Pt pad was grown by scanning a 35 μm × 7.5 μm region with a 286 pA, 30 keV electron beam for 40 minutes under a flowing mixture of $Pt(PF_3)_4$ and XeF_2. The beam was maintained scanning during Pt deposition, but the electron flux was sufficiently low to make the direct EBID rate[14,15,23,24,27–31] negligible. The deposit is highly pure (i.e., indistinguishable from pure Pt within the detection limits of EDS), and exhibits porosity that spans nano- to microscopic length scales. The structure seen in the scanning transmission electron microscopy (STEM) images in Figure 2C-D is consistent with the AFM profiles in Figure 1B. It is analogous to that of Pt black and Pt sponge,[19–22] and distinctly different from that of the comparatively smooth, continuous EBID-grown Pt.[27–31] Transmission electron microscopy (TEM) images and selected area diffraction (SAD) patterns show that the material is nanocrystalline, fcc Pt with a crystallite diameter of $\sim$ 3 nm (Figure 2E). Cracks such as those seen in Figure 2C and D were observed in thick films and are attributed to relaxation of high residual stresses in the deposits. Film growth took place at high rates and room temperature, where adatom mobility is low and can result in high film stresses that increase with film thickness. Film stress is typically concentrated at defects sim-

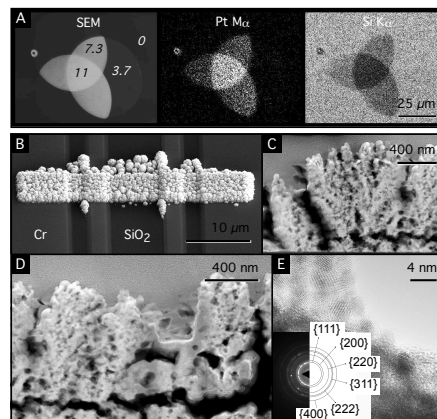ilar to the pores, which likely mediate crack propagation through the deposits.

Figure 2. A) SEM image and EDS maps of Pt deposits grown on three pre-patterned circular, overlapping surface regions. The mean pre-patterning fluence was 11, 7.3, 3.7 and 0 electrons/$Å^2$. B) An SEM image, (C,D) STEM images, and (E) a TEM image and a SAD pattern of a Pt deposit grown on a substrate comprised of SiO_2 and Cr electrodes.

Pt film localization was also achieved by 30 keV Ga$^+$ beam pre-exposure of the substrates under flowing XeF_2. This is not surprising since ion irradiation causes adsorbate dissociation[38] in a manner analogous to electron irradiation. The process is, however, complicated by ion induced surface roughening and amorphization, and is therefore not discussed here in detail.

We now turn to an analysis of the surface functionalization (i.e., fluorination) process which leads to Pt nucleation and enables beam directed localization. A mixture of XeF_2 and $Pt(PF_3)_4$ is expected to decompose to solid Pt and gaseous byproducts through fluorine-induced decomposition of $Pt(PF_3)_4$ and thermal desorption of Xe and PF_x adsorbates[40–42] (where the desorption rate increases as x is increased from 3 to 5). To show that the experimental Pt nucleation time scales with calculated reciprocal concentration of adsorbed F, we used a model of XeF_2 adsorption and dissociation in the presence of energetic electrons. It is based on a general model of physisorption and activated chemisorption[43] which we adapted for the case of XeF_2 molecules on SiO_2 as described in the Supporting Information.

Figure 3A is a schematic illustration of the physisorbed XeF_2 and chemisorbed F states considered by the model. The reaction coordinate is distance away from the substrate surface, and fluorination is assumed to proceed primarily through dissociation of physisorbed XeF_2 molecules as discussed in the Supporting Information. Parts B and C of the figure show plots of F and XeF_2 coverage (i.e., fractional occupation of the chemisorbed and physisorbed states, each limited to one monolayer). The coverages were calculated at room temperature as a function of time after the SiO_2 substrate is exposed to XeF_2 vapor. The initial coverages were set to zero, and the times it takes F coverages to saturate represent reciprocal surface functionalization rates.
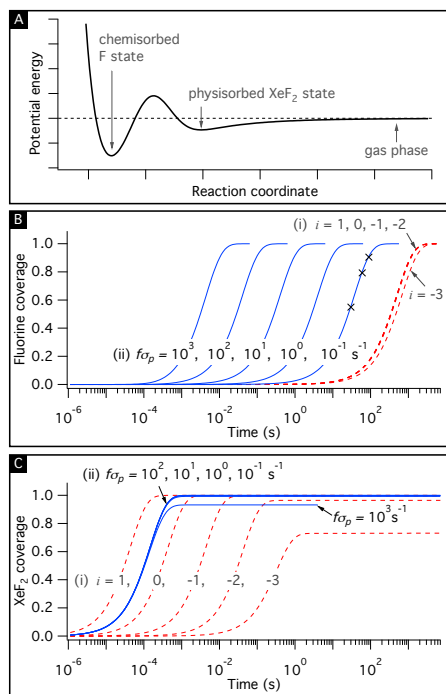
Figure 3. A) Schematic one dimensional potential energy diagram for XeF_2 physisorption and activated chemisorption. B,C) F and XeF_2 coverage calculated as a function of time under these conditions: (i) no electron exposure [(- - - -), $s_pP = 1.3 \times 10^i$ Pa, where i = -3 to 1 step 1], and (ii) with electron dissociation of XeF_2 enabled [(——), $f\sigma_p = 10^{-1}$ to 10^3 s^{-1}; $s_pP = 4$ Pa]. Markers ($\times$) indicate F coverage at electron beam exposure times of 30, 60 and 90 s [$f\sigma_p = 10^{-1}$ s^{-1}].

Beam-free functionalization was simulated using s_pP values in the range of 10^{-3} to 10 Pa, where s_p is the sticking coefficient for XeF_2 physisorption, P is pressure and the s_pP values encompass the range encountered in our experiments, as discussed in the Supporting Information. Chemisorbed F coverage takes thousands of seconds to saturate at all pressures considered in the calculations (see the curves labelled (i) in Figure 3B). Conversely, the XeF_2 coverage saturation time is much shorter (10^{-4} to 1 s; Figure 3C) and a strong function of pressure. This behavior is expected since XeF_2 physisorption is rate-limited by the gas molecule arrival rate from vacuum, and the physisorbed XeF_2 coverage rapidly saturates at each pressure. The chemisorption rate is slower because it is limited by dissociation of XeF_2 molecules, which is governed primarily by the height of the activation barrier between the physisorbed and chemisorbed states shown in Figure 3A.

Electron beam functionalization was simulated using $f\sigma_p$ values in the range of 10^{-1} to 10^3 s^{-1}, where f is electron flux and σ_p is the effective cross-section for electron dissociation of physisorbed XeF_2 molecules. The model shows that electron irradiation causes a dramatic decrease in the fluorination time, even under conditions of very low electron flux (see the curves labelled (ii) in Figure 3B). Hence, electron beam exposure of SiO_2 in an XeF_2 environment is expected to cause very efficient, rapid fluorination of the surface. An example that we can compare to experiment is provided by the curve calculated using $f\sigma_p = 10^{-1}$ s^{-1}, which approximates the conditions used to generate the partially overlapping circles in Figure 2A. The curve yields F coverages of $\sim$ 0.55, 0.79 and 0.91 at exposure times of 30, 60 and 90 s, respectively. These times correspond to the three regions of zero, single and double overlap which are seen in Figure 2A as regions of progressively elevated Pt concentration. The correlation between measured Pt concentration (Figure 2A) and calculated F coverage (markers ($\times$) in Figure 3B) is consistent with the interpretation that the Pt nucleation

time scales with reciprocal fluorine coverage.

The data in Figure 3B also show that the measured Pt concentration does not scale with physisorbed XeF_2 coverage. At electron fluxes used in the experiments, XeF_2 coverage is governed by the XeF_2 adsorption rate from the gas phase. At very high electron fluxes ($f\sigma_p \gtrsim 10^3$ s^{-1}), the coverage *decreases* with f (due to rapid consumption of XeF_2 through electron induced dissociation) and can not explain the nucleation behavior observed experimentally.

The above simulation results are consistent with the hypothesis that Pt nucleation is induced by chemisorbed fluorine. Both the theory and experiments indicate that the beam-free growth process is scalable and can potentially be used for deposition of large area films by controlled, uniform delivery of $Pt(PF_3)_4$ and XeF_2 to macroscopic substrates. The process is solvent-free, applicable to both conducting and insulating substrates and occurs at room temperature. It is therefore compatible with a wide range of substrates, as well as photoresist microfabrication and lift-off techniques that are typically used for lithography of wafer-scale electrodes. Substrates may optionally be functionalized by (delocalized) electron flood exposure, or using a highly focused electron beam. The former may improve the throughput of large area deposition, while the latter enables direct-writing of Pt for nano-prototyping. The autocatalysis of Pt growth observed after nucleation suggests that the as-grown films and nanoparticles are well suited to a wide range of applications.

In summary, we developed a method for the synthesis of highly porous, nanocrystalline platinum based on fluorine-induced decomposition of $Pt(PF_3)_4$ adsorbates. Spatial localization was achieved by functionalizing substrates by charged particle beams. The Pt nucleation time was shown to scale with reciprocal fluorine coverage by a combination of experiment and a rate kinetics model of XeF_2 dissociation on SiO_2.

Experimental Section

Pt deposition was carried out in a FEI Company Quanta 3D field emission gun (FEG) Dual Beam modified to enable simultaneous delivery of XeF_2 and $Pt(PF_3)_4$ vapors into the specimen chamber. The solid XeF_2 and liquid $Pt(PF_3)_4$ precursors were housed externally in separate stainless steel vapor delivery systems equipped with pressure-feedback motorized leak valves that enable accurate, independent control of precursor flow rates into the vacuum chamber. Each vapor was routed independently to a gas injection capillary with an inner diameter of 500 μm, that could be positioned freely during SEM imaging (Figure 1A). The gases were not premixed and interacted only after exiting their respective capillaries. Three substrates were used to investigate the deposition process: Si with a native oxide, thermally grown SiO_2, and SiO_2 with pre-patterned Cr electrodes. Typical background partial pressures of $Pt(PF_3)_4$ and XeF_2 were $\sim 10^{-3}$ Pa and 3×10^{-3} Pa, respectively. The corresponding maximum local pressures at the substrate surface were approximately three orders of magnitude greater than the background pressures.[44] $Pt(PF_3)_4$ has previosly been used as a precursor for chemical vapor deposition,[42,45] laser beam deposition,[16] and EBID.[27–31] We performed EBID using a 5 keV, 3.4 nA electron beam.

SEM imaging and EDS analysis were done in-situ using an Everhart-Thornley secondary electron detector, and an Oxford Instruments INCA EDS system. Ex-situ analysis was performed on samples that had been transferred in air, using TEM, high angle annular dark field (HAADF) STEM and SAD using an FEI Titan. Lamella for TEM analysis were prepared using conventional

ion beam preparation and liftout[46] techniques. Surface morphology was characterized in air by tapping mode AFM performed with etched silicon probes installed on a Dimension DI-3100 AFM.

Notes and References

(1) Kloke, A.; von Stetten, F.; Zengerle, R.; Kerzenmacher, S. *Adv. Mater.* **2011**, *23*, 4976–5008.

(2) Chen, A.; Holt-Hindle, P. *Chem Rev* **2010**, *110*, 3767–3804.

(3) Attard, G. S.; Bartlett, P. N.; Coleman, N. R. B.; Elliott, J. M.; Owen, J. R.; Wang, J. H. *Science* **1997**, *278*, 838–840.

(4) Ding, Y.; Chen, M. W.; Erlebacher, J. *J. Am. Chem. Soc.* **2004**, *126*, 6876–6877.

(5) Kloke, A.; Koehler, C.; Gerwig, R.; Zengerle, R.; Kerzenmacher, S. *Adv. Mater.* **2012**, *24*, 2916–2921.

(6) Steele, B. C. H.; Heinzel, A. *Nature* **2001**, *414*, 345–352.

(7) Ralph, T. R.; Hogarth, M. P. *Platinum Metals Rev* **2002**, *46*, 3–14.

(8) Korotcenkov, G.; Do Han, S.; Stetter, J. R. *Chem Rev* **2009**, *109*, 1402–1433.

(9) Stetter, J. R.; Li, J. *Chem Rev* **2008**, *108*, 352–366.

(10) Astruc, D.; Lu, F.; Aranzaes, J. R. *Angew Chem Int Edit* **2005**, *44*, 7852–7872.

(11) Murzin, D. Y.; Maki-Arvela, P.; Toukoniitty, E.; Salmi, T. *Catal Rev* **2005**, *47*, 175–256.

(12) Mailley, S.; Hyland, M.; Mailley, P.; McLaughlin, J. A.; McAdams, E. T. *Bioelectrochemistry* **2004**, *63*, 359–364.

(13) Cheung, K. C. *Biomed Microdevices* **2007**, *9*, 923–938.

(14) Randolph, S. J.; Fowlkes, J. D.; Rack, P. D. *Cr. Rev. Solid State* **2006**, *31*, 55–89.

(15) Utke, I.; Hoffmann, P.; Melngailis, J. *J. Vac. Sci. Technol. B* **2008**, *26*, 1197–1276.

(16) Schroder, H.; Kompa, K. L.; Masci, D.; Gianinoni, I. *Appl Phys A-Mater* **1985**, *38*, 227–233.

(17) Hayase, M.; Fujii, T.; Alves Brito-Neto, J. G. *Journal of The Electrochemical Society* **2011**, *158*, B355.

(18) Brault, P.; Caillard, a.; Thomann, a. L.; Mathias, J.; Charles, C.; Boswell, R. W.; Escribano, S.; Durand, J.; Sauvage, T. *Journal of Physics D: Applied Physics* **2004**, *37*, 3419–3423.

(19) Benton, A. F. *J. Am. Chem. Soc.* **1926**, *48*, 1850–1861.

(20) Feltham, A. M.; Spiro, M. *Chem Rev* **1971**, *71*, 177–193.

(21) Guo, S.; Fang, Y.; Dong, S.; Wang, E. *J Phys Chem C* **2007**, *111*, 17104–17109.

(22) Marrese, C. A. *Anal Chem* **1987**, *59*, 217–218.

(23) Van Dorp, W. F.; Hagen, C. W. *J. Appl. Phys.* **2008**, *104*, 081301.

(24) Botman, A.; Mulders, J. J. L.; Hagen, C. W. *Nanotechnology* **2009**, *20*, 372001.

(25) Utke, I.; Michler, J.; Gasser, P.; Santschi, C.; Laub, D.; Cantoni, M.; Buffat, P. A.; Jiao, C.; Hoffmann, P. *Adv. Eng. Mater.* **2005**, *7*, 323–331.

(26) Hoeflich, K.; Yang, R. B.; Berger, A.; Leuchs, G.; Christiansen, S. *Adv. Mater.* **2011**, *23*, 2657–2661.

(27) Wang, S.; Sun, Y.-M. M.; Wang, Q.; White, J. M. *J. Vac. Sci. Technol. B* **2004**, *22*, 1803–1806.

(28) Barry, J. D.; Ervin, M.; Molstad, J.; Wickenden, A.; Brintlinger, T.; Hoffman, P.; Meingailis, J. *J. Vac. Sci. Technol. B* **2006**, *24*, 3165–3168.

(29) Botman, A.; Hesselberth, M.; Mulders, J. J. L. *Microelectronic Engineering* **2008**, *85*, 1139–1142.

(30) Botman, A.; Hagen, C. W.; Li, J.; Thiel, B. L.; Dunn, K. A.; Mulders, J. J. L.; Randolph, S.; Toth, M. *J. Vac. Sci. Technol. B* **2009**, *27*, 2759–2763.

(31) Landheer, K.; Rosenberg, S. G.; Bernau, L.; Swiderek, P.; Utke, I.; Hagen, C. W.; Fairbrother, D. H. *J. Phys. Chem. C* **2011**, *115*, 17452–17463.

(32) The P K_α peak overlaps with Pt M_α, causing broadening of the low energy side of the net peak seen in the figure.

(33) The conditioning treatment had to be repeated each time gas flow was terminated and the chamber was left in high vacuum for more than $\sim$3 hours, or if a vent cycle was performed, likely due to F interactions with H_2O and O_2.

(34) Winters, H. F.; Coburn, J. W. *Appl. Phys. Lett.* **1979**, *34*, 70–73.

(35) Tu, Y. Y.; Chuang, T. J.; Winters, H. F. *Phys. Rev. B* **1981**, *23*, 823–835.

(36) Loudiana, M. A.; Schmid, A.; Dickinson, J. T.; Ashley, E. J. *Surf. Sci.* **1984**, *141*, 409–416.

(37) Hills, M. M.; Arnold, G. S. *Appl. Surf. Sci.* **1991**, *47*, 77–90.

(38) Coburn, J.; Winters, H. *J. Appl. Phys.* **1979**, *50*, 3189–3196.

(39) Randolph, S.; Toth, M.; Cullen, J.; Chandler, C.; Lobo, C. *Appl. Phys. Lett.* **2011**, *99*, 213103.

(40) Goldberg, I. B.; Crowe, H. R.; Pilipovich, D. *Chem. Phys. Lett.* **1975**, *33*, 347–350.

(41) Nitschke, F.; Ertl, G.; Kuppers, J. *J. Chem. Phys.* **1981**, *74*, 5911–5921.

(42) Zhang, R.; Comita, P. B. *Chem Phys Lett* **1992**, *200*, 297–302.

(43) Bishop, J.; Lobo, C. J.; Martin, A.; Ford, M.; Phillips, M.; Toth, M. *Phys. Rev. Lett.* **2012**, *109*, 146103.

(44) Friedli, V.; Utke, I. *J. Phys. D* **2009**, *42*, 125305.

(45) Rand, M. J. *J. Electrochem. Soc.* **1973**, *120*, 686–693.

(46) Giannuzzi, L.; Stevie, F. *Micron* **1999**, *30*, 197–204.